Commun Nonlinear Sci Numer Simulat 150 (2025) 109024

Contents lists available at ScienceDirect

Communications in Nonlinear Science and Numerical Simulation

journal homepage: www.elsevier.com/locate/cnsns

Research paper

Multistability and complexity in the planar spin–orbit problem

Vitor M. de Oliveira *

Instituto de Matemática e Estatística, Universidade de São Paulo, São Paulo, 05508-090, Brazil
CFisUC, Departamento de Física, Universidade de Coimbra, Coimbra, 3004-516, Portugal

ARTICLE INFO

Keywords:
Celestial mechanics
Chaos
Tides
Spin–orbit coupling

ABSTRACT

The tidal evolution of a deformable body may lead to a state where its rotational and orbital motion are in resonance. In this work, we numerically investigate and visually illustrate some dynamical properties of the dissipative spin–orbit problem, namely, the co-existence of multiple periodic and quasi-periodic attractors, and the complexity of the corresponding basins of attraction. We apply our methodology first to Hyperion, and later to the Moon and Mercury. Our results provide a visual aid to understand the complicated dynamics of the system, and show that the different dynamical scenarios in this problem can be well characterized by the Gibbs entropy.

1. Introduction

Many natural satellites in the Solar System, including the Moon, possess an orbital period similar to their rotational period. These bodies probably rotated much faster upon their formation and then went through a despinning process due to tidal interactions with their massive companions [1,2], until eventually ending up in a synchronous rotation. Since the seminal work by Darwin [3], many authors have studied the rotational dynamics of orbiting bodies under the effect of tidal forces [4–8]. These forces are stronger in orbiting bodies that are bigger or closer to the central body [9], but they can also lead to spin synchronization in small bodies such as secondaries of binary asteroids in the main belt [10].

The closest planet to the Sun, Mercury, is currently in a 3/2 spin–orbit resonance, i.e., it takes the same amount of time to rotate around its spin axis thrice as it takes to revolve around the Sun twice [11]. This discovery showed that a two-body system can be locked into other configurations besides the synchronous one, which has lead to many works regarding the final state of tidally evolved systems. In particular, an analytical probability for a planet or satellite to be captured into a spin–orbit resonance based on arguments about energy dissipation was derived [12], that was then reinterpreted in terms of Adiabatic Invariant Theory [13]. Later, it was showed that the chaotic evolution of Mercury's orbit could have driven its orbital eccentricity high enough during the planet's history so that the probability of it ending up in its current state was actually higher than previously thought [14].

From a dynamical systems perspective, we can interpret the probability of a given trajectory being captured by a resonance as the probability of a random trajectory converging to a certain final state in the phase space. The final state is then an attractor in the system. In a system with multistability, i.e., many co-existing attractors, such concept can be related to the size of the basin of attraction associated with each attractor [15,16]. For example, when tidal dissipation acts on a rotating triaxial body, the location of its Cassini states changes, and some of these solutions become attractors with their own basins of attraction [17]. Here, we are interested in visually illustrating and also quantifying the complexity of the basins of attraction in the spin–orbit problem. To carry on with this investigation, we choose a low-dimensional model of the problem which assumes that the orbiting body rotates perpendicularly to the orbit plane, and that it follows a Keplerian orbit with fixed parameters. We then determine the basins of

---

* Correspondence to: Instituto de Matemática e Estatística, Universidade de São Paulo, São Paulo, 05508-090, Brazil.
E-mail address: vitormo@ime.usp.br.

https://doi.org/10.1016/j.cnsns.2025.109024
Received 24 June 2024; Received in revised form 20 May 2025; Accepted 27 May 2025

Available online 16 June 2025
1007-5704/© 2025 Elsevier B.V. All rights are reserved, including those for text and data mining, AI training, and similar technologies.

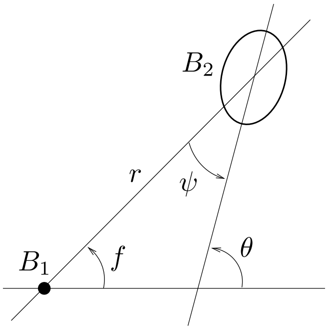

Fig. 1. Schematic of the system. The body B_2 orbits body B_1 following a Keplerian orbit. f is the true anomaly, θ the rotation angle, and $\psi = \theta - f$.

attraction of the main resonances, and we measure their respective sizes and entropy for a range of orbital eccentricities. With this, we depict the intricate structure formed by the basins of attraction in the spin–orbit problem, and we evaluate how dominating the probability of converging to a final state is over the others via the Gibbs entropy, which are the main contributions of this work. Our results highlight the rich dynamical scenarios that may emerge from such a system.

This paper is organized as follows. In Section 2 we present the equations of motion for our physical model. Later, in Section 3 we briefly expose the main ideas regarding the Gibbs entropy in our context. The dynamical analyses for Hyperion, the Moon, and Mercury are presented in Sections 4 and 5. Finally, in Section 6 we give some general remarks and state our conclusions.

2. Physical model

Our physical model consists in an orbiting body B_2 that revolves around a central body B_1 with the following considerations: the orbit is given by a fixed Keplerian ellipse with eccentricity e, semi-major axis a, mean motion n, and instantaneous radius r; B_1 is a point mass whilst B_2 is an extended triaxial body with principal moments of inertia $A < B < C$; the orbiting body's spin-axis is parallel to C and perpendicular to the orbit plane; and the only forces acting on B_2 are due to the gravitational field generated by B_1. We illustrate the system in Fig. 1.

We are interested here in the rotational dynamics of B_2, and in its relation to the body's orbital motion. The position of the orbiting body along its trajectory may be determined by the true anomaly f, and its rotation may be evaluated by the angle θ between the axis along A (largest physical axis) and a coordinate axis fixed in the inertial space, which we take to intersect both the central body and the point of periapsis. We also consider that B_1 raises a tide on the orbiting body, which we assume to be almost rigid. The time lag between the distortion of the body and the tide-raising potential is assumed to be constant [18,19], which leads to a dissipation function that is linear on the body's relative angular velocity $\dot{\psi}$ [20,21].

With the aforementioned considerations, we can derive an equation for the rotational dynamics of B_2, which is given by[1]

$$C\ddot{\theta} = -\frac{3}{2}(B - A)\frac{Gm_1}{r^3}\sin 2\psi - \frac{\Gamma}{r^6}\dot{\psi}, \tag{1}$$

where G is the gravitational constant and m_1 is the mass of B_1. The first term on the right-hand side of Eq. (1) is the gravitational torque due to the body's triaxiality ($B \neq A$), while the second term is the dissipative tidal torque caused by the deformation of B_2. The orbital motion of B_2 is embedded in the instantaneous radius r and in the true anomaly f, both of which are functions of time.

By rearranging the terms in Eq. (1) and defining the equatorial oblateness as $\gamma = 3(B - A)/2C$, our equation of motion can be rewritten as[2]

$$\ddot{\theta} = -\gamma \frac{Gm_1}{r^3}\sin 2(\theta - f) - K\left(L\dot{\theta} - N\right), \tag{2}$$

where

$$L = \frac{a^6}{r^6} \quad \text{and} \quad N = \frac{a^8}{r^8} n\sqrt{1 - e^2},$$

and where we have used $r^2\dot{f} = na^2\sqrt{1 - e^2}$ [9]. We call K the *dissipation constant*.

A spin–orbit resonance corresponds to a state where the number of orbits of B_2 around B_1, and the number of rotations of B_2 around its spin-axis, are commensurable. If T is the orbital period, a *spin–orbit resonance* (SOR) of type p/q is a solution for the system such that [16]

$$\theta(t + Tq) = \theta(t) + 2\pi p \qquad \text{for all} \qquad t \in \mathbb{R}, \tag{3}$$

---

[1] The constant Γ is given by $3k_2 G m_1^2 R^5 \tau$, where R is the satellite's radius, τ is the time lag, and k_2 is the Love number [22].

[2] The equation of motion for the planar dissipative spin–orbit problem is usually written in this manner since both L and N have simple time averages which are valid for small values of eccentricity [20]. In here, however, we use the non-averaged equation.

with p and $q > 0$ integers.

Spin–orbit resonances are, by definition, periodic orbits. If B_2 is in one of these resonances, it expends the same amount of time to orbit around the central body q times and to spin around itself p times. For $K = 0$, Eq. (2) describes an one-and-a-half degree of freedom near integrable conservative system, with both γ and e as perturbation parameters. Therefore, the system can possess a mixed phase space, with the coexistence of regular and chaotic motion [23]. For $K > 0$, some spin–orbit resonances may become *periodic attractors*, being the final state of a set of trajectories with positive measure. We call the set of initial conditions that converge in time to a given attractor the *basin of attraction* of said solution [24].

Eq. (2) may also possess solutions of the form

$$\theta(t) = \omega t + u(\omega t, t) \qquad \text{for all} \qquad t \in \mathbb{R}, \tag{4}$$

where ω is irrational, and $u(\varphi_1, \varphi_2)$ is T-periodic in φ_1 and φ_2. Such orbits form KAM curves in the conservative case and may become *quasi-periodic attractors* in the dissipative case [25].

In order to help us analyze the spin–orbit problem, we define a *stroboscopic map* $\mathbf{M}$ which acts on the system's phase space as $(\theta(t), \dot{\theta}(t)) \rightarrow (\theta(t+T), \dot{\theta}(t+T))$. With this definition, we reduce the three-dimensional continuous system to a two-dimensional autonomous discrete system. Note that the spin–orbit resonances are represented on $\mathbf{M}$ by periodic orbits with period q, while the quasi-periodic solutions are represented by one-dimensional curves.

The model presented in this Section is well established and was used to study spin–orbit coupling in many works [14,16,26,27]. The fact that it is a low-dimensional model gives us access to numerical tools that are capable of visually illustrating the dynamical properties of orbits in the phase space.

3. Entropy

The basin of attraction of a given attractor is the portion of the phase space whose initial conditions lead to orbits that converge to this attractor. Hence the size of the basin of attraction can be interpreted as the probability of a random initial condition to belong in said basin. In multistable systems, multiple basins coexist and their basins compete for room in the phase space. In this situation, the individual basin sizes give the probability of a random initial condition to converge to each final state. Although very relevant, this information alone does not reflect how dynamically complex the phase space is. More specifically, it does not show how the phase space is divided among the basins.

In order to infer some information on that matter, we use the Gibbs entropy S, which is defined as [28]

$$S = \sum_{i=1}^{N_A} p_i \ln\left(\frac{1}{p_i}\right), \tag{5}$$

where N_A is the number of attractors, and p_i is the probability of a given orbit to belong to the basin of attraction of the i-th attractor.

The entropy S assembles in a single number the information on how heterogeneous the basin sizes are. In particular, when all basins have the same size, $p_i = p = 1/N_A$, the entropy is maximum. In this situation, we obtain from Eq. (5)

$$S_{max} = \ln N_A. \tag{6}$$

Conversely, if $S \ll S_{max}$, it means that one of the basins has a size much larger than all of the others. Hence, the entropy reflects how dominant an attractor may be in the phase space, i.e., how much more probable one final state is over the others. This information also takes into consideration the total number of attractors N_A in the system, whose value might depend on the system parameters.

It is worth mentioning that a measure derived from S called basin entropy was previously introduced by other authors [29]. This measure is dependent on the grid resolution utilized to analyze the phase space, and it can be used to obtain information on basin boundaries and for classifying basins of attraction [30]. For example, it can determine an uncertainty exponent which is related to the fractality of the basin boundaries [29,31]. Here, we use S itself as a measure for the system's complexity.

4. Hyperion

Hyperion is a moon of Saturn that has long been considered the primary example in the Solar System of a body possibly exhibiting a chaotic rotational state [26,32].[3] This natural satellite has a highly aspherical shape, being nearly twice as long as it is across, with orbital eccentricity and equatorial oblateness given by $e_{hyp} = 0.1$ and $\gamma_{hyp} = 0.396$, respectively [34]. In this section, we adopt these parameters in order to study the spin–orbit problem.

We carry out our investigation by integrating Eq. (2). For all of our simulations, we begin the orbital motion of the satellite at *periapsis*, i.e., $f(t=0) = 0$ and $r(t=0) = a(1-e)$, and we calculate $r(t)$ by integrating Newton's gravitational equation at each time-step. We also take $a = 1$ and $T = 2\pi$, which leads to $n = 1$ and $Gm_1 = 1$. Numerical integration is performed via an explicit embedded Runge–Kutta Prince-Dormand 7(8) scheme with adaptive step-size control [35].

---

[3] A recent study using a more general model which does not impose planar or principal axis rotation suggests that Hyperion is not tumbling chaotically, but rather rotating quasi-regularly [33].

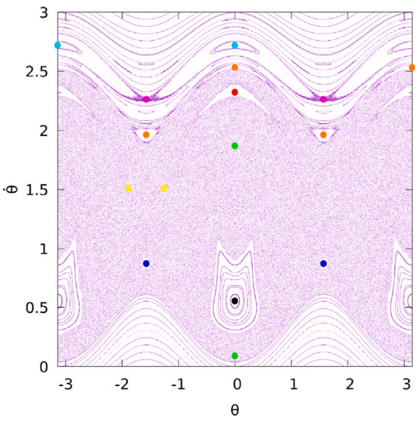

Fig. 2. Hyperion's phase space with the main SORs. 1/1 stable (black), 2/1 stable (red), 1/2 stable (dark blue), 2/2 unstable (green), 3/2 unstable (yellow), 5/2 stable (light blue), 5/2 unstable (pink), and 9/4 stable (orange).

4.1. Conservative scenario

Let us first consider the case where Hyperion is treated as a rigid body and, consequently, there is no tidal dissipation in the satellite's rotation. In this case, we have $K = 0$, and the gravitational torque is the only term present in Eq. (2). Fig. 2 shows the system's phase space $\theta \times \dot{\theta}$ calculated on the stroboscopic map $\mathbf{M}$, from where we can observe a typical near-integrable Hamiltonian system scenario, with regions of regular motion coexisting with chaos.

The location of a few low-order spin–orbit resonances (SORs) are also marked in Fig. 2 by colored points. We determine these periodic orbits with an accuracy of $\sim 10^{-10}$ using a numerical routine to select good candidates in the phase space, along with an iterative minimization procedure [36]. For a SOR of type p/q, the value of q reflects the period of the orbit on $\mathbf{M}$, while p is the number of rotations measured outside the surface of section after q intersections.

The stability of the periodic orbits in Fig. 2 is determined via linear stability analysis. Since the stroboscopic map is well defined, we can numerically calculate the Jacobian matrix of the mapping after q iterations, for which a periodic orbit of period q is a fixed point. For the conservative case, the eigenvalues of the Jacobian matrix are complex numbers if the fixed point is stable, while they are real numbers if the fixed point is unstable. Later, when dissipation is considered, the stability of the periodic orbit will be given by the magnitude of these eigenvalues [24].

We are interested in understanding how the phase space changes as we vary the physical parameters of the system. In Fig. 3, we present the phase space for different values of the orbital eccentricity e inside a given range. All panels were generated using the same initial conditions, which are marked by green dots. What we observe is the system going from a pendulum-like regular motion to a mixed phase space as the value is increased. During this process, some SORs bifurcate, changing stability, and regions of regular motion vary in size. For even larger values of e, the depicted region of the phase space is almost fully covered by chaotic orbits.[4]

4.2. Time series with tidal dissipation

When we consider Hyperion as an almost rigid body, tidal dissipation comes into play and some of the spin–orbit resonances become attractors. However, as we showed in Fig. 3, the system's dynamical scenario vastly changes as we vary the orbital eccentricity. In Fig. 4, the evolution of the angular velocity $\dot{\theta}$ is shown as a function of the number of orbital periods T_n (the unity of time in $\mathbf{M}$) for different values of e, and for the same initial condition in all cases, namely, $\theta(0) = 0.0$ and $\dot{\theta}(0) = 1000.0$ rad/u.t., where u.t. stands for unit of time (i.e., Hyperion facing Saturn while rapidly spinning). We choose a dissipation constant of $K = 10^{-2}$, a value which is high enough so we may observe the effects that tidal dissipation has on the system in a reasonable amount of simulation time, and low enough so that the interesting dynamical phenomena are not totally suppressed by the dissipation.

Two conclusions can be taken from Fig. 4. First, the discrete-time series is composed by three parts: an exponential decay, an erratic motion, and an asymptotic state corresponding to a resonance. Second, varying the value of the eccentricity affects the time series mostly in two manners: it changes the slope corresponding to the initial exponential decay, and it possibly modifies the system's final state, i.e., to which SOR the trajectory eventually converges. The chaotic nature of the conservative phase space translates as chaotic transients when dissipation is considered. This can be seen in the erratic portion of the time series in Fig. 4.

---

[4] An investigation on the resonances in this model is carried out in Ref. [37] for low orbital eccentricities ($e = 0.01$ and $e = 0.02$) and different values of the equatorial oblateness ($\gamma \in [0.0,\ 1.125]$), where a comparison between an analytical approach via perturbative treatments and a numerical approach via dynamical indicators is performed.

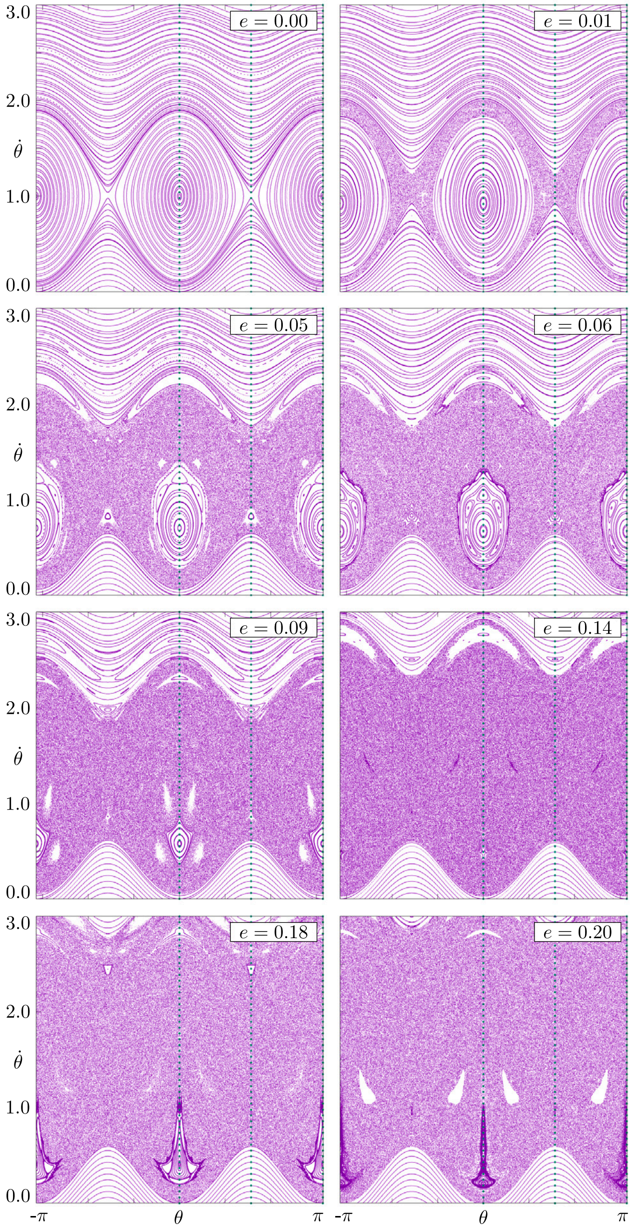

Fig. 3. Phase space for $\gamma = \gamma_{hyp}$, $K = 0$, and different values of e. The initial conditions chosen for these figures are marked by green dots.

Hence, the system still exhibits sensitive dependence on initial conditions, i.e., initial conditions that are close together can lead to very different trajectories, which might converge to different SORs [15].

Chaotic orbits can also mimic dynamical aspects of unstable periodic orbits inside the chaotic sea for a limited amount of time. Consequently, a trajectory on the phase space can become temporarily trapped around attractors during its chaotic transient. In order to illustrate this behavior, we show the phase space trajectory in Fig. 5 that corresponds to the time series for $e = 0.140$ in Fig. 4. The orbit is superimposed in the conservative phase space for reference, and the colorbar indicates the number of orbital periods T_n (discrete time) for each point in the orbit. At about $T_n = 1000$ (red points), the trajectory approaches a $1/1$ SOR and starts to revolve around it. However, instead of converging to this resonance, the orbit moves away and eventually converges to a $5/4$ SOR (yellow points).

Both dynamical aspects mentioned before, namely, sensitive dependence on initial conditions and temporary entrapment around periodic orbits, are related to invariant manifolds of unstable periodic orbits [38,39]. These geometrical structures permeate the

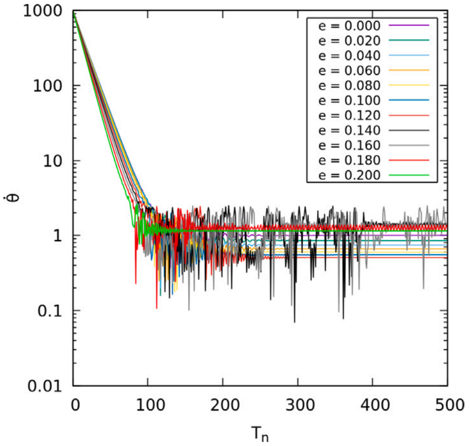

Fig. 4. Discrete-time series for a trajectory on **M** beginning at $\theta(0) = 0.0$ and $\dot{\theta}(0) = 1000.0$ rad/u.t., $K = 10^{-2}$, $\gamma = \gamma_{hyp}$, and different values of e.

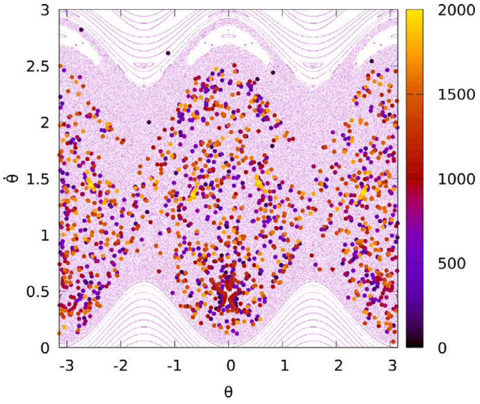

Fig. 5. Phase space trajectory beginning at $\theta(0) = 0.0$ and $\dot{\theta}(0) = 1000.0$ rad/u.t., for $K = 10^{-2}$, $\gamma = \gamma_{hyp}$, and $e = 0.140$ (black curve in Fig. 4). The color in each point of the orbit corresponds to the number of orbital periods T_n as given by the colorbar. The conservative phase space is shown in the background for reference.

Table 1
Basin sizes and entropy for $e = e_{hyp}$, $\gamma = \gamma_{hyp}$, and $K = 10^{-2}$.

Basin size			Entropy
1/1	2/1	1/2	
89.94%	8.00%	2.06%	0.344

phase space, bending and crossing each other, and render the system dynamics very complex. They also play an important role in the spin–orbit resonance capture, since they form the boundaries of the basins of attraction [31].

4.3. Basins of attraction for Hyperion

As defined before, the set of trajectories that converge in time to an attractor compose its basin of attraction. In order to visually illustrate the basins of attraction for Hyperion, we selected a square grid of 600 × 600 initial conditions in the phase space, evolved the equations of motion for each one, Eq. (2), and then determined their final state, later associating a color to each type of SOR. The results are shown in Fig. 6. The basin sizes, which are based on the number of points on the grid that compose each of them, along with the system entropy, are presented in Table 1. Here, there are three SORs, namely, 1/1, 1/2, and 2/1, and it is possible to observe two aspects: the boundaries between the basins are complex, as indicated by the fine visual structures in the figure, and the basin of the synchronous resonance (1/1 SOR) dominates the phase space, as indicated by the low entropy.

The information on Fig. 6 and Table 1 indicate that, if Hyperion's orbital eccentricity e_{hyp} remains constant, the synchronous resonance is its most probable final rotational state, given that this attractor dominate the phase space. However, the complex boundaries between the basins suggest that a prediction is hard, and that any perturbation might eventually lead the trajectory to another SOR.

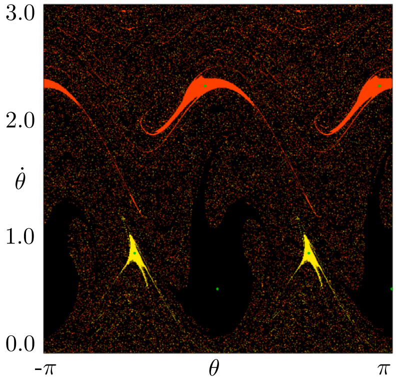

Fig. 6. Basins of attraction for Hyperion with dissipation constant given by $K = 10^{-2}$. The color code corresponds to the following SORs: 1/1 (black), 2/1 (orange), and 1/2 (yellow). The locations of the SORs are marked with little green dots.

In Fig. 7, we maintain the values for γ and K used in Fig. 6, and we calculate the basins of attraction of SORs for the same range of e as in Fig. 3. For $e = 0$, the 1/1 SOR is the only resonance present and hence its basin of attraction (in black) completely fills the phase space. As the value for the orbital eccentricity is increased, other attractors appear along with their basins (multistability). It is possible to observe that the basins of attraction are intertwined with each other in the phase space, which highlights the complex dynamical scenario of the system. For $e = 0.2$, the synchronous resonance has bifurcated (period-doubling), giving origin to a 2/2 SOR (basin in gray). Note that the 2/2 SOR is different from the 1/1 SOR, since this solution only closes after the body fully rotates around itself two times, which takes two orbital periods.

By comparing Figs. 3 to 7, we are able to observe the effect the tidal dissipation has on the system. While most of the stable periodic orbits in the conservative case are destroyed when dissipation is applied, some of these become periodic attractors in the dissipative case, each with its own basin of attraction. For example, with $e = 0.06$, the attractors are the 1/1, 2/1, 1/2 and 4/4 spin–orbit resonances, and with $e = 0.18$, the attractors are the 1/1, 1/2, 5/2, and 5/4 SORs. Another comparison between the two cases can be made concerning stable and unstable invariant manifolds associated with unstable periodic orbits. These geometrical structures are embedded in the chaotic sea of the conservative case and their crossings lead to the chaotic behavior of nearby orbits. In the dissipative case, structures such as these form the boundaries between the basins, and their crossings are responsible for chaotic transients.

We are treating here different attractors that correspond to the same type of SOR as effectively the same attractor, i.e., we combine the basins of all attractors with the same p and q. For example, if the orbiting body is in the synchronous solution, it only shows the same side to the central body. However, there is another synchronous solution, where the orbiting body would always show its other side to the central body. We consider both these final states to be the same since they lead to the same physical outcome.

In Fig. 8, we plot the size of the basins of attraction as a function of the orbital eccentricity e. We call higher-order (HO) resonances all SORs with $p > 9$ or $q > 4$. As observed in Fig. 7, the basin size for the synchronous resonance dominates for lower values of eccentricity ($e \leq 0.05$). At $e = 0.01$, in particular, the 3/2 SOR exists, it is stable, and its basin of attraction has a small size. However, the basin for the synchronous resonance competes for space with other basins as the eccentricity increases, especially at $e = 0.09$ and $e = 0.14$, where the probability of a random trajectory to converge to the 1/1 spin–orbit resonance falls to approximately 0.6 and 0.4, respectively. For these parameters, the 4/4 SOR ($e = 0.09$), and the 5/4 and 1/2 SORs ($e = 0.14$) also become probable outcomes.

We also show in Fig. 8 the entropy at each orbital eccentricity. The most striking outcome is the correlation between the value of the system's entropy and the basin size of the SOR with lowest order. As the orbital eccentricity changes, the entropy varies and such variation inversely follows the tendency of the 1/1 SOR basin size. For $e > 0.18$, the synchronous resonance is not stable anymore, and the entropy starts to follow the 2/2 SOR. These results highlight the important role of lower order resonances in the system dynamics.

5. Moon & Mercury

We now apply our methodology to investigate the rotational dynamics of both the Moon and Mercury. As before, we adopt the system described in Section 2 as our model, and we numerically integrate the equations of motion given by Eq. (2). We set the orbital eccentricities of the Moon and Mercury as $e_{Moon} = 0.0549$ and $e_{Mercury} = 0.2056$, and we choose a dissipation parameter of $K = 10^{-4}$. In both cases, we adopted an equatorial oblateness of $\gamma = 10^{-4}$.

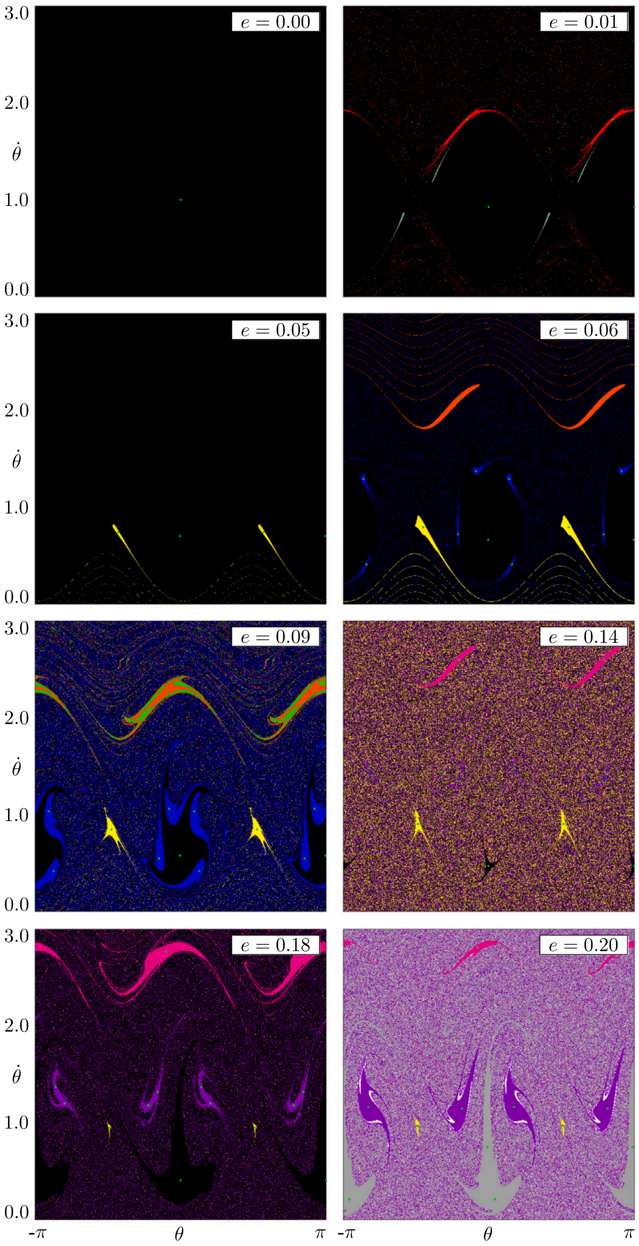

Fig. 7. Basins of attraction for $K = 10^{-2}$, $\gamma = \gamma_{hyp}$, and different values of e. The color code corresponds to the following SORs: 1/1 (black), 2/1 (orange), 1/2 (yellow), 2/2 (gray), 3/2 (red), 4/2 (dark-green), 5/2 (pink), 4/4 (blue), 5/4 (violet), and 8/4 (green). The basin of higher-order resonances ($p > 9$ or $q > 4$) is white, and the locations of the SORs are marked with little green dots.

5.1. *Winding number*

The main physical aspect that differentiates both the Moon and Mercury from Hyperion is that they possess a very spherical shape, which leads to a somewhat distinct dynamical scenario. In particular, we observe the presence of quasi-period attractors (see Eq. (4)). In order to distinguish between this type of solution and a spin–orbit resonance, we calculate the attractor's *winding number* ω, which is defined as

$$\omega = \lim_{n\to\infty} \frac{\theta_n - \theta_0}{n}, \tag{7}$$

for a given discrete-time orbit $\{\theta_0, \theta_1, \dots\}$ in $\mathbf{M}$.

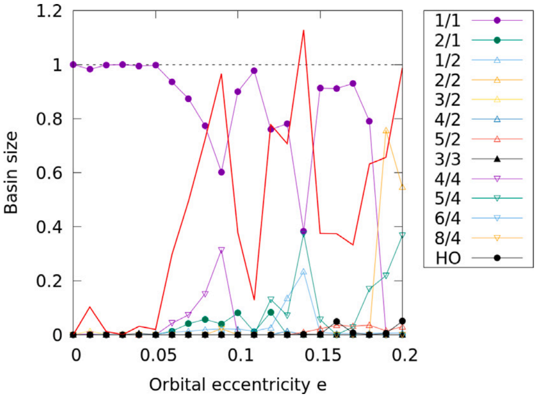

Fig. 8. Size of the basins of attraction and entropy (red curve) as a function of the orbital eccentricity for $\gamma = \gamma_{hyp}$ and $K = 10^{-2}$. HO stands for higher-order SORs ($p > 9$ or $q > 4$).

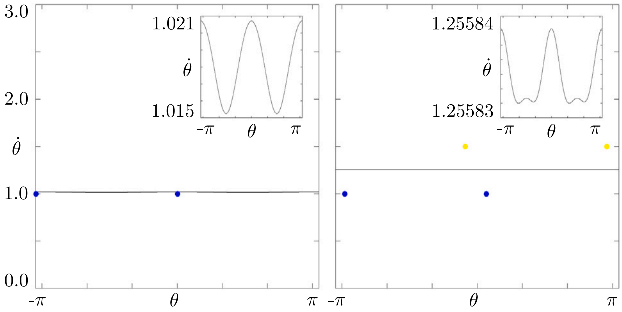

Fig. 9. Attractors for (left) $e = e_{Moon}$ and (right) $e = e_{Mercury}$. Blue dots mark 1/1 SORs, yellow dots mark 3/2 SORs, and the quasi-periodic attractors are formed by the black curves. Inlet graphs show a magnification of these solutions, whose winding numbers are given by $\omega \approx 1.01788$ for the Moon and $\omega \approx 1.25584$ for Mercury.

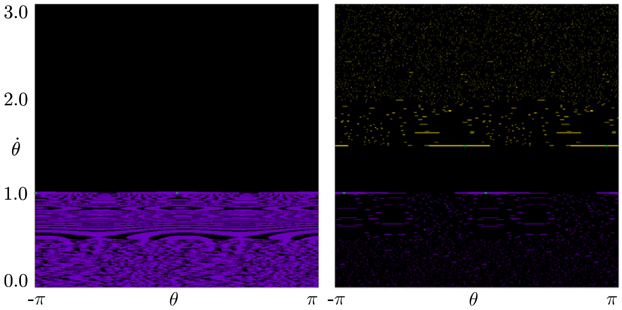

Fig. 10. Basins of attraction for (left) $e = e_{Moon}$ and (right) $e = e_{Mercury}$. Dissipation constant and equatorial oblateness are given by $K = 10^{-4}$ and $\gamma = 10^{-4}$, respectively. The color code corresponds to the following attractors: quasi-periodic (black), 1/1 (purple), and 3/2 (yellow). The locations of the SORs are marked with little green dots.

Periodic orbits have a rational winding number while KAM tori have an irrational winding number [40]. Therefore, it is possible to determine if an orbit converged to a periodic attractor or to a quasi-periodic attractor by measuring its winding number, and then determining to a certain precision if it corresponds to a rational or an irrational number. In Fig. 9, we present the attractors for the Moon (left) and for Mercury (right). While the system for $e = e_{Moon}$ has a quasi-periodic attractor co-existing with the synchronous resonance (blue dots), for $e = e_{Mercury}$ the system has a quasi-periodic attractor co-existing with both the synchronous and the 3/2 SOR (yellow dots).

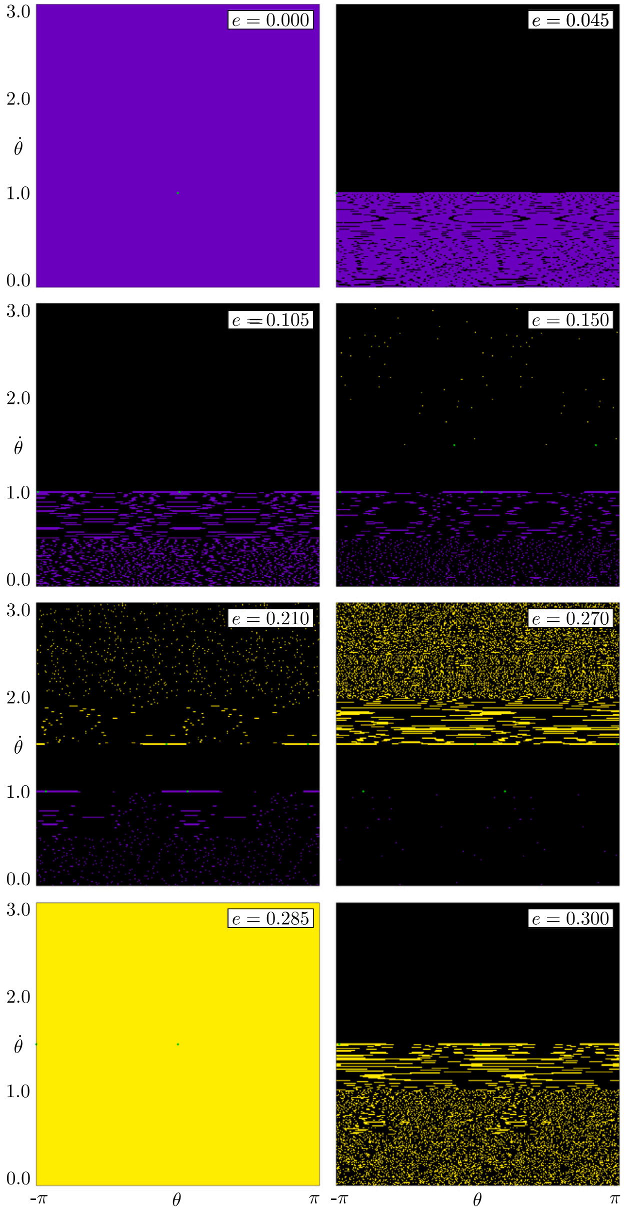

Fig. 11. Basins of attraction for $K = 10^{-4}$, $\gamma = 10^{-4}$, and different values of e. The color code corresponds to the following attractors: quasi-periodic (black), 1/1 (purple), and 3/2 (yellow). The locations of the SORs are marked with little green dots.

5.2. Basins of attraction for Moon and Mercury

In Fig. 10, we present the basins of attraction for the Moon (left) and Mercury (right). Here we set a fixed step size for the numerical integration scheme, and we calculated the basin of attraction on a square grid of 300 × 300 initial conditions. The basin of the quasi-periodic attractor is shown in black, and the basins for the $1/1$ and $3/2$ SORs are painted purple and yellow, respectively.

While the Moon contains only the synchronous resonance besides the quasi-periodic attractor, which means that these are the only two final states available in the system, Mercury also contains the $3/2$ SOR. The associated basin sizes and entropy are shown in Table 2. Even though both situations present an intricate basin structure, the quasi-periodic attractor dominates the phase space for $e = e_{Mercury}$, and hence the entropy is smaller in comparison to the Moon, where the synchronous resonance also fills a large area of the phase space. We can also observe from Fig. 10 that, for Mercury, the basin of attraction associated with the quasi-periodic attractor separates the other two basins in the phase space, in the same manner as KAM tori act as barriers in the conservative system. With this, there is no basin boundary between the synchronous resonance and the 3/2 SOR for Mercury and, consequently,

Table 2
Basin sizes and entropy for $\gamma = 10^{-4}$, $K = 10^{-4}$, and the eccentricities of the Moon (e_{Moon}) and Mercury ($e_{Mercury}$).

e	Basin size			Entropy
	1/1	3/2	Quasi-periodic	
e_{Moon}	22.13%		77.87%	0.529
$e_{Mercury}$	1.38%	1.17%	97.45%	0.136

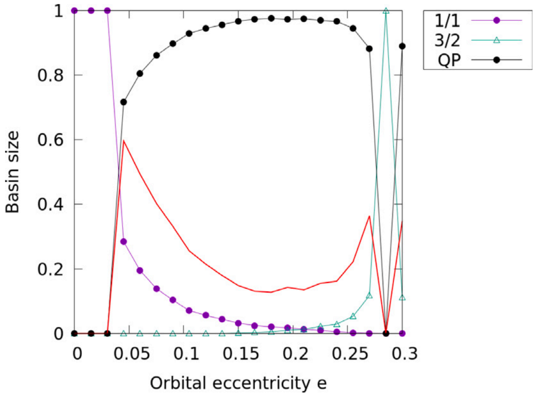

Fig. 12. Size of the basins of attraction for $K = 10^{-4}$ and $\gamma = 10^{-4}$, where QP stands for quasi-periodic attractors. The entropy is shown in red.

a perturbed orbit inside the 3/2 basin would have to go through the quasi-periodic basin before possibly reaching the synchronous basin.

In Fig. 11, we maintain $\gamma = 10^{-4}$ and $K = 10^{-4}$, and we depict the basins of attraction for different values of e. As before, the basin of the quasi-periodic solutions are shown in black, while the basin for the synchronous resonance is painted purple, and the one for the 3/2 SOR is painted yellow. The basin sizes and the corresponding entropy are shown in Fig. 12. For $e = 0.0$, as expected, the synchronous resonance completely fills the phase space. For $e = 0.045$, a quasi-periodic orbit appears and its basin dominates the phase space. As the orbital eccentricity is increased, the basin of the 3/2 SOR steadily grows, until finally covering all the phase space at $e = 0.285$, where both the synchronous resonance and the quasi-periodic attractor disappear. After that, another quasi-periodic attractor appears along with its basin, which in turn competes for space with the 3/2 SOR basin.

6. Conclusions

In this work, we have visually illustrated the basins of attraction for the dissipative spin–orbit problem, considering the parameters of Hyperion at first, and later the parameters for the Moon and Mercury. In all cases, the basins presented an intricate structure, being highly intertwined with one another. The visual depiction of the system's complexity was complemented by the Gibbs entropy in each case, a measure that reflects the heterogeneity of the basin sizes, and that was shown to be correlated to the dominant attractor in the phase space, i.e., the most probable final state in the system.

For Hyperion, the probability of a trajectory ending up in a synchronous rotation not only varies considerably as a function of the orbital eccentricity, but also the 1/1 SOR itself bifurcates and changes stability, rendering such final state impossible for e higher than a critical value. For the Moon and Mercury, where the equatorial oblateness is lower, quasi-periodic attractors appear. For values of e where both the synchronous solution and the 3/2 SOR exist, their basin of attraction are separated by the basin that belongs to the quasi-periodic attractor, which almost always dominate the phase space.

Even though the Gibbs entropy does not provide the full picture, knowing how heterogeneous the system's phase space is could help us understand why a certain system is in a given state. For example, in our physical model, Mercury has a low entropy for its current parameters as a consequence of the large basin of attraction associated with a quasi-periodic attractor. This supports the idea that Mercury was probably captured in the 3/2 spin–orbit resonance when it was in a dynamical configuration where the basin of such a resonance was larger [14].

It is also worth noting that the Gibbs entropy investigated here can be easily extended to higher-dimensional physical models, which is important since it is harder, if not impossible, to visually describe these types of systems. For example, the case of Mercury in the 3/2 spin–orbit resonance considering a full three-dimensional model. Additionally, the Gibbs entropy is well suited for Monte-Carlo simulations. Since it is a measure that combines the sizes of all the basins of attraction, when we estimate it via Monte-Carlo simulations it means we also have an estimation for all of the basin sizes. Hence, we can estimate all of the quantities of interest with one numerical procedure (see Appendix).

In the future, we intend to use a more realistic rheological model [7], and analyze how changes in the equatorial oblateness, which are due to long term variations of spin and tidal forces, might affect the topology of the basins of attraction.

Table A.3
Basin sizes and entropy for $\gamma = 10^{-4}$ and $e = e_{Moon}$.

K	Basin size				Entropy
	1/1	3/2	QP	Other SORs	
10^{-4}	21.64%		78.36%		0.522
10^{-5}	0.91%	0.41%	98.68%		0.079
10^{-6}	0.85%	0.61%	97.91%	0.63%	0.134

Table A.4
Basin sizes and entropy for $\gamma = 10^{-4}$ and $e = e_{Mercury}$.

K	Basin size				Entropy
	1/1	3/2	QP	Other SORs	
10^{-4}	1.21%	1.27%	97.52%		0.133
10^{-5}	0.94%	0.43%	98.28%	0.35%	0.105
10^{-6}	0.54%	0.65%	97.07%	1.74%	0.187

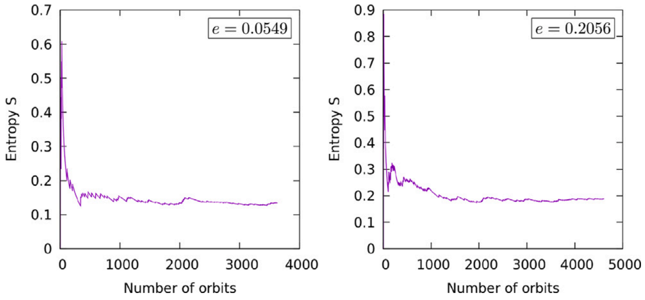

Fig. A.13. Entropy as a function of the total number of randomly selected orbits for $\gamma = 10^{-4}$, $K = 10^{-6}$, (left) $e = e_{Moon}$, and (right) $e = e_{Mercury}$..

CRediT authorship contribution statement

Vitor M. de Oliveira: Writing – original draft, Software, Methodology, Investigation, Funding acquisition, Formal analysis, Conceptualization.

Declaration of competing interest

The authors declare that they have no known competing financial interests or personal relationships that could have appeared to influence the work reported in this paper.

Acknowledgments

We like to thank Clodoaldo Ragazzo for his comments and suggestions, and Project Gutenberg for making a book referenced in this article available online. We also like to thank the anonymous reviewers who helped improve this work. This work was partially supported by the São Paulo Research Foundation (FAPESP, Brazil), under Grants No. 2021/11306-0 and 2022/12785-1, and by Fundação para a Ciência e a Tecnologia (FCT, Portugal), under projects UIDP/04564/2020[5] and UIDB/04564/2020.[6]

Appendix. Monte Carlo simulations for lower dissipation values

The dissipation constant sets the timescale for energy loss in the system. Lower values of K means that orbits in the phase space take longer to converge on average, and hence computational time can become prohibitive in this situation. However, it is often possible to obtain results using Monte-Carlo simulations, since these require less initial conditions than over-the-grid calculation in order to measure a given quantity. In fact, we did compare our results to Monte-Carlo simulations, for which we obtained similar conclusions. A Monte-Carlo simulation is faster, but the uniform grid method allows us to visually depict the basins of attraction more easily, which is the focus of our work.

---

[5] https://doi.org/10.54499/UIDP/04564/2020.

[6] https://doi.org/10.54499/UIDB/04564/2020.

In Tables A.3 (Moon) and A.4 (Mercury), we present the basin sizes and the entropy for values of K equal and lower than the one adopted in Section 5. In each simulation, we selected initial conditions at random following a uniform distribution, evolved them in time, and calculated an estimative for the entropy for every new orbit. We then stopped the procedure if the entropy value changed less than 10^{-2} in a window of 1000 new orbits (see Fig. A.13). In the regime of lower dissipation constant values, there are more stable solutions and, consequently, more basins of attraction that compete for space. However, in almost all scenarios, the basins of attraction of quasi-period attractors almost completely dominated the considered region of the phase space.

Data availability

Data will be made available on request.

References

[1] MacDonald GJF. Tidal friction. Rev Geophys 1964;2(3):467–541.
[2] Kokubo E, Ida S. Formation of terrestrial planets from protoplanets. II. Statistics of planetary spin. Astrophys J 2007;671(2):2082.
[3] Darwin GHI. On the bodily tides of viscous and semi-elastic spheroids, and on the ocean tides upon a yielding nucleus. Philos Trans R Soc Lond 1879;(170):1–35.
[4] Efroimsky M. Bodily tides near spin–orbit resonances. Celest Mech Dyn Astron 2012;112(3):283–330.
[5] Ferraz-Mello S. Tidal synchronization of close-in satellites and exoplanets. A rheophysical approach. Celest Mech Dyn Astron 2013;116(2):109–40.
[6] Correia AC, Boué G, Laskar J, Rodríguez A. Deformation and tidal evolution of close-in planets and satellites using a maxwell viscoelastic rheology. Astron Astrophys 2014;571:A50.
[7] Ragazzo C, Ruiz LS. Viscoelastic tides: models for use in Celestial mechanics. Celest Mech Dyn Astron 2017;128(1):19–59.
[8] Correia ACM, Delisle J-B. Spin–orbit coupling for close-in planets. Astron Astrophys 2019;630:A102.
[9] Murray CD, Dermott SF. Solar system dynamics. United Kingdom: Cambridge University Press; 1999.
[10] Goldreich P, Re'em S. Tidal evolution of rubble piles. Astrophys J 2009;691(1):54.
[11] Pettengill G, Dyce R. A radar determination of the rotation of the planet Mercury. Nature 1965;206:1240.
[12] Goldreich P, Peale S. Spin–orbit coupling in the solar system. Astron J 1966;71:425.
[13] Henrard J. Spin–orbit resonance and the adiabatic invariant. In: Resonances in the motion of planets, satellites and asteroids. 1985, p. 19–26.
[14] Correia ACM, Laskar J. Mercury's capture into the 3/2 spin–orbit resonance as a result of its chaotic dynamics. Nature 2004;429(6994):848–50.
[15] Ott E. Chaos in dynamical systems. Cambridge: Cambridge University Press; 2002.
[16] Celletti A, Chierchia L. Measures of basins of attraction in spin–orbit dynamics. Celest Mech Dyn Astron 2008;101:159–70.
[17] Bills BG, Brown AJ. Influence of energy dissipation on spin pole precession trajectories for synchronous rotators. Planet Sci J 2022;3(1):18.
[18] Singer SF. The origin of the moon and geophysical consequences. Geophys J Int 1968;15(1–2):205–26.
[19] Mignard F. In: The evolution of the lunar orbit revisited. I, The Moon and the planets, vol. 20, no. 3, 1979, p. 301–15.
[20] Peale SJ. The free precession and libration of Mercury. Icarus 2005;178(1):4–18.
[21] Efroimsky M, Lainey V. Physics of bodily tides in terrestrial planets and the appropriate scales of dynamical evolution. J Geophys Res: Planets 2007;112(E12).
[22] Love AEH. A treatise on the mathematical theory of elasticity. Cambridge: Cambridge University Press; 1927.
[23] Lichtenberg AJ, Lieberman MA. Regular and chaotic dynamics, applied mathematical sciences. New York: Springer-Verlag; 1992.
[24] Alligood KT, Sauer TD, Yorke JA. Chaos: An introduction to dynamical systems. Textbooks in mathematical sciences, New York: Springer; 2012.
[25] Celletti A, Chierchia L. Quasi-periodic attractors in celestial mechanics. Arch Ration Mech Anal 2009;191:311–45.
[26] Wisdom J, Peale SJ, Mignard F. The chaotic rotation of hyperion. Icarus 1984;58(2):137–52.
[27] A. Celletti C Lhotka. Transient times, resonances and drifts of attractors in dissipative rotational dynamics. Commun Nonlinear Sci Numer Simul 2014;19(9):3399–411.
[28] Gibbs JW. Elementary principles in statistical mechanics: developed with especial reference to the rational foundation of thermodynamics. Cambridge library collection - mathematics, Cambridge: Cambridge University Press; 1902, http://dx.doi.org/10.1017/CBO9780511686948.
[29] Daza A, Wagemakers A, Georgeot B, Guéry-Odelin D, Sanjuán MA. Basin entropy: a new tool to analyze uncertainty in dynamical systems. Sci Rep 2016;6(1):1–10.
[30] Daza A, Wagemakers A, Sanjuán MA. Classifying basins of attraction using the basin entropy. Chaos Solitons Fractals 2022;159:112112.
[31] Grebogi C, McDonald SW, Ott E, Yorke JA. Final state sensitivity: an obstruction to predictability. Phys Lett A 1983;99(9):415–8.
[32] Wisdom J. Rotational dynamics of irregularly shaped natural satellites. Astron J 1987;94:1350–60.
[33] Goldberg M, Batygin K. Nutation-orbit resonances: The origin of the chaotic rotation of Hyperion and the barrel instability. Astron Astrophys 2024;692:A9.
[34] Wisdom J. Urey prize lecture: Chaotic dynamics in the solar system. Icarus 1987;72(2):241–75.
[35] Galassi M, Gough B, Rossi F, Theiler J, Jungman G, Booth M, et al. GNU scientific library: reference manual. Surrey: Network Theory Limited; 2001.
[36] Raphaldini B, Ciro D, Medeiros ES, Massaroppe L, Trindade RIF. Evidence for crisis-induced intermittency during geomagnetic superchron transitions. Phys Rev E 2020;101(2):022206.
[37] Lei H. Dynamical structures associated with high-order and secondary resonances in the spin–orbit problem. Astron J 2024;167(3):121.
[38] de Oliveira VM, Ciro D, Caldas IL. Dynamical trapping in the area-preserving Hénon map. Eur Phys J Spec Top 2020;229(8):1507–16.
[39] de Oliveira VM, Palmero MS, Caldas IL. Measure, dimension, and complexity of the transient motion in Hamiltonian systems. Phys D: Nonlinear Phenom 2022;431:133126.
[40] Reichl L. The transition to chaos: conservative classical systems and quantum manifestations. New York: Springer; 2004.